



## Origin of misorientations for fcc→hcp transformation in pure cobalt and its in-situ validation

Jin-jiang HE<sup>1,2</sup>, Guo-jin XU<sup>1,2</sup>, Xing-quan WANG<sup>3</sup>, Jun-feng LUO<sup>1,2</sup>, Dan LIU<sup>1,2</sup>, Yong-jun LI<sup>1,2</sup>, Xin-fu GU<sup>4</sup>

1. GRIKIN Advanced Material Co., Ltd., Beijing 102200, China;

2. Beijing Technology Research Center for Sputtering Target Material Engineering of High Pure Metals, Beijing 102200, China;

3. China GRINM Group Co., Ltd., Beijing 102200, China;

4. School of Materials Science and Engineering, University of Science and Technology Beijing, Beijing 100083, China

Received 5 September 2023; accepted 25 April 2024

**Abstract:** The origin of the misorientations after fcc (face-centered cubic) to hcp (hexagonal close-packed) transformation in pure cobalt was elucidated by utilizing the electron backscatter diffraction (EBSD) technique and transformation crystallographic models. It is found the Shoji–Nishiyama orientation relationship during fcc→hcp transformation leads to four hcp variants, characterized by a common misorientation angle of 70.5° with respect to the  $\langle 11\bar{2}0 \rangle$  direction, which is the predominant misorientation observed. Other statistically significant misorientation angles between hcp grains, including 32°, 36°, 38°, 60°, 71° and 86°–91°, are also identified. These newly observed misorientation angles are linked to the microstructure of the fcc matrix at elevated temperatures, with twin structures in the fcc matrix being the primary cause. Furthermore, a novel method is proposed for estimating the fraction of twins in the fcc grains based on misorientation angles between hcp variants, which is found to be consistent with experimental observations. In-situ EBSD observations validate the possible origin of fcc twins from the hcp→fcc transformation.

**Key words:** cobalt; transformation crystallography; variant; orientation relationship; twin

### 1 Introduction

Cobalt and cobalt alloys play a crucial role in various applications, including implants, magnetic media, connectors for integrated circuits, etc. [1–4]. This significance is attributed to their favourable characteristics such as good corrosion resistance, magnetic properties, and biocompatibility. Pure cobalt commonly undergoes an allotropic transformation between fcc (face-centered cubic) and hcp (hexagonal close-packed), i.e. fcc↔hcp transformation, around 420 °C [5], and the hcp structure is stable at lower temperature.

During the fcc↔hcp transformation, a low-energy interface is established between the fcc and hcp structures to minimize the energy barrier associated with the phase transformation, leading to a reproducible orientation relationship between these two phases. Specifically, this relationship is known as the Shoji–Nishiyama orientation relationship [6]:

$$\begin{aligned} \{111\}_{\text{fcc}} // \{0001\}_{\text{hcp}} \\ \langle \bar{1}01 \rangle_{\text{fcc}} // \langle 2\bar{1}\bar{1}0 \rangle_{\text{hcp}} \end{aligned}$$

The interface is parallel to  $\{111\}_{\text{fcc}} // \{0001\}_{\text{hcp}}$ . This orientation relationship is easy to understand due to the similarity in the atomic structure within

**Corresponding author:** Jun-feng LUO, Tel: +86-10-80103388, E-mail: [ljf@grikin.com](mailto:ljf@grikin.com);

Xin-fu GU, Tel: +86-10-82376968, E-mail: [xinfugu@ustb.edu.cn](mailto:xinfugu@ustb.edu.cn)

[https://doi.org/10.1016/S1003-6326\(25\)66765-3](https://doi.org/10.1016/S1003-6326(25)66765-3)

1003-6326/© 2025 The Nonferrous Metals Society of China. Published by Elsevier Ltd & Science Press

This is an open access article under the CC BY-NC-ND license (<http://creativecommons.org/licenses/by-nc-nd/4.0/>)

the  $\{111\}_{\text{fcc}}//\{0001\}_{\text{hcp}}$  close-packed planes. It is worth noting that the  $\text{fcc}\leftrightarrow\text{hcp}$  transformation is considered as an athermal process [7] and the transformation proceeds with the movement of partial dislocations, specifically  $1/6\langle 112 \rangle_{\text{fcc}}$  or  $1/3\langle 1\bar{1}00 \rangle_{\text{hcp}}$  [5,8,9].

The transformed hcp product exhibits parallel plates or plates intersecting at a special angle, forming a regular pattern [10]. The distinctive pattern arises from the crystallographic equivalent hcp variants associated with the Shoji–Nishiyama orientation relationship. It has been observed that a single crystal can possess four variants by heating and quenching study [11]. The commonly reported misorientation angle is approximately  $70.5^\circ$  [10,12–17], consistent with the misorientation angle between the plates as determined by the electron backscatter diffraction (EBSD) method. Grain boundaries featuring this misorientation are recognized as special boundaries. Despite the frequent reporting of  $70.5^\circ$  misorientation, it is important to note the existence of other misorientations, notably around  $40^\circ$  and  $60^\circ$ . Consequently, further exploration of these special boundaries and misorientations is necessary to gain a comprehensive understanding of the microstructure formed during the  $\text{fcc}\rightarrow\text{hcp}$  transformation. Additionally, understanding the boundary characteristics is crucial for controlling boundary stability [18], including the anisotropic migration rate of the interface either in phase transformation or recrystallization [19], etc.

Furthermore, it is not only pure cobalt that experiences the  $\text{fcc}\leftrightarrow\text{hcp}$  phase transformation, but also cobalt alloys [7,20–22], steels [23–25], high entropy alloys [26–28], Co binder in cemented carbide [17,29–31], etc. The occurrence of the  $\text{fcc}\leftrightarrow\text{hcp}$  transformation serves as a valuable system for comprehending both the transformation microstructure and the plastic deformation mechanism, commonly referred to as transformation-induced plasticity (TRIP). Consequently, the  $\text{fcc}\leftrightarrow\text{hcp}$  transformation is simple but of great technical importance.

This study aims to provide a quantitative explanation for the origin of the misorientation distribution between the hcp grains. Additionally, a novel mechanism for fcc twins resulting from  $\text{hcp}\rightarrow\text{fcc}$  transformations is proposed, and its validation is conducted through in-situ EBSD

observations. Beyond the conventional annealing twins, the transformation twins offer a new way for grain boundary engineering for the system exhibiting  $\text{hcp}\rightarrow\text{fcc}$  transformations.

## 2 Experimental

In this study, high-purity cobalt (99.999%, 5N) was used, subjected to heat treatment at  $550^\circ\text{C}$  for 1 h, followed by furnace cooling to room temperature. As shown in Fig. 1, obtained by the differential scanning calorimetry (DSC) with a heating/cooling rate of  $10^\circ\text{C}/\text{min}$ , the transformation initiates around  $426^\circ\text{C}$  and finishes at about  $469.5^\circ\text{C}$ . Consequently, a full fcc phase is anticipated at  $550^\circ\text{C}$ , facilitating the examination of the nature of  $\text{fcc}\rightarrow\text{hcp}$  transformation. The samples were cut, mechanically ground, polished at 10 V and 120 mA, and finally etched by 4% Nital etchant for microstructure characterization. The microstructure observations were conducted through scanning electron microscopy (ZEISS Gemini 2) with an electron backscatter diffraction (EBSD) system (Oxford Symmetry2). The in-situ EBSD test was carried out with an in-situ heater (MINI-HT750-EBSD, Qiyue Tech.) and compared with the microstructure at room temperature to unveil the transformation rules of  $\text{hcp}\rightarrow\text{fcc}$  during heating. The heating temperature for the in-situ observation was set up to  $450^\circ\text{C}$ , allowing simultaneous presence of fcc and hcp phases, providing insight into the transformation crystallographic features between two phases. The EBSD data were processed and reconstructed using the AZtecCrystal software (Oxford Instruments),

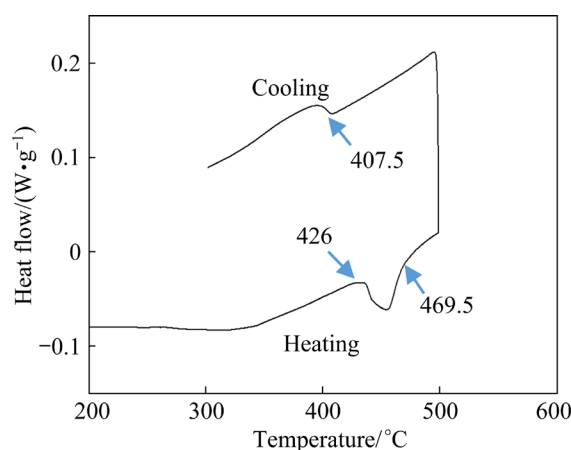


**Fig. 1** DSC curve with heating and cooling rate of  $10^\circ\text{C}/\text{min}$

and the transformation crystallography was analyzed using the open-source software PTCLab [32].

### 3 Results and discussion

#### 3.1 Orientation variants

The orientation relationship between the fcc and hcp phases typically obeys the Shoji–Nishiyama orientation relationship [6], owing to the similarity in atomic structure within the close-packed planes of both phases. Due to the symmetry of the parent fcc phase, there are four equivalent expressions of this orientations, as outlined in Table 1. These four equivalent orientations are referred to as orientation variants [33]. It is noteworthy that the variants in more complex systems can be generated by matrix operations [33,34] or software like PTCLab [32].

**Table 1** Four crystallographic variants for Shoji–Nishiyama orientation relationship

No.	Close packed plane	Close packed direction
V <sub>1</sub>	(111) <sub>fcc</sub> //(0001) <sub>hcp</sub>	$[\bar{1}01]_{fcc}//[2\bar{1}\bar{1}0]_{hcp}$
V <sub>2</sub>	( $\bar{1}\bar{1}1$ ) <sub>fcc</sub> //(0001) <sub>hcp</sub>	$[101]_{fcc}//[2\bar{1}\bar{1}0]_{hcp}$
V <sub>3</sub>	(1 $\bar{1}\bar{1}$ ) <sub>fcc</sub> //(0001) <sub>hcp</sub>	$[011]_{fcc}//[2\bar{1}\bar{1}0]_{hcp}$
V <sub>4</sub>	(11 $\bar{1}$ ) <sub>fcc</sub> //(0001) <sub>hcp</sub>	$[\bar{1}10]_{fcc}//[2\bar{1}\bar{1}0]_{hcp}$

The four hcp variants highlighted in red and parent fcc shown in blue are depicted in Fig. 2. In Fig. 2(a), the distribution of the variants along the  $[001]_{fcc}$  direction is illustrated, where the four variants V<sub>1</sub>–V<sub>4</sub> align with the four-fold symmetry axis ( $[001]_{fcc}$ ) in the parent fcc structure. Similarly, Fig. 2(b) shows the projection of variants along  $[111]_{fcc}$  direction, with the four variants conforming to the three-fold symmetry axis ( $[111]_{fcc}$ ) in the parent fcc structure. These finds demonstrate that the four orientation variants can be systematically generated through the symmetry operations of the parent fcc phase. Generally, the variant number is less than the number of symmetry operations in the fcc structure, as the number of orientation variants also depends on the orientation relationship itself [33]. For instance, the three-fold symmetry axis from two structures coincides with each other at the Shoji–Nishiyama orientation relationship, i.e.  $\{111\}_{fcc}//\{0001\}_{hcp}$ , but no new orientation variants from the orientation relationship,  $(111)_{fcc}//(0001)_{hcp}$  and  $[\bar{1}01]_{fcc}//[2\bar{1}\bar{1}0]_{hcp}$ , will be generated through

the rotation around the three-fold symmetry axis  $[111]_{fcc}$ .

According to Fig. 2, the deviation between the four variants can be characterized as a 90° rotation around  $\langle 001 \rangle_{fcc}$  axis in Fig. 2(a) or a 120° rotation around  $\langle 111 \rangle_{fcc}$  axis in Fig. 2(b). In the EBSD analysis, the smallest deviation, i.e. the misorientation angle, is typically evaluated to avoid ambiguities. The smallest deviation can be calculated by considering the symmetry of the hcp phase [35], and the resulting misorientation angle is determined to be 70.5° around  $\langle 011 \rangle$  axis, as illustrated in Fig. 3. The variants V<sub>1</sub> and V<sub>2</sub> (Table 1) are shown in Fig. 3, i.e.  $(111)_{fcc}//(0001)_{hcp}$  and  $(\bar{1}\bar{1}1)_{fcc}//(0001)_{hcp}$ , and the deviation between these two variants equals the angle between the  $[111]_{fcc}$  and  $[\bar{1}\bar{1}1]_{fcc}$  directions, i.e. 70.5°. Similar relationships exist for other variant pairs, and the misorientation angle between arbitrary two from four variants is consistently 70.5°, and the misorientation axis is along  $\langle 011 \rangle$  in fcc and  $\langle 11\bar{2}0 \rangle$  in hcp according to Fig. 3.

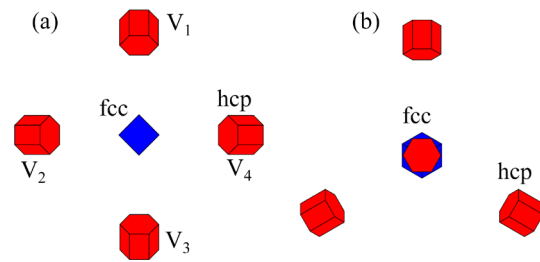


**Fig. 2** Distribution of four hcp variants: (a)  $[001]_{fcc}$  view; (b)  $[111]_{fcc}$  view (The blue lattice is the parent fcc structure, and the red lattices are four hcp variants with Shoji–Nishiyama orientation relationship)

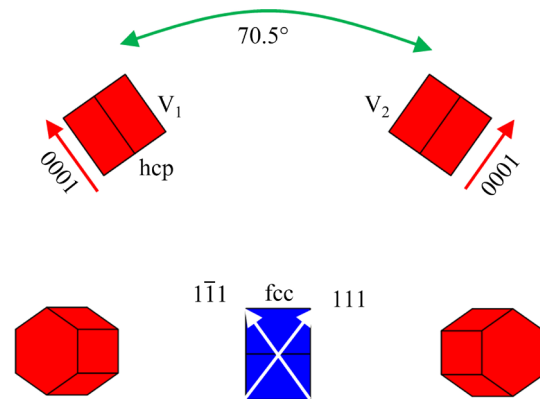
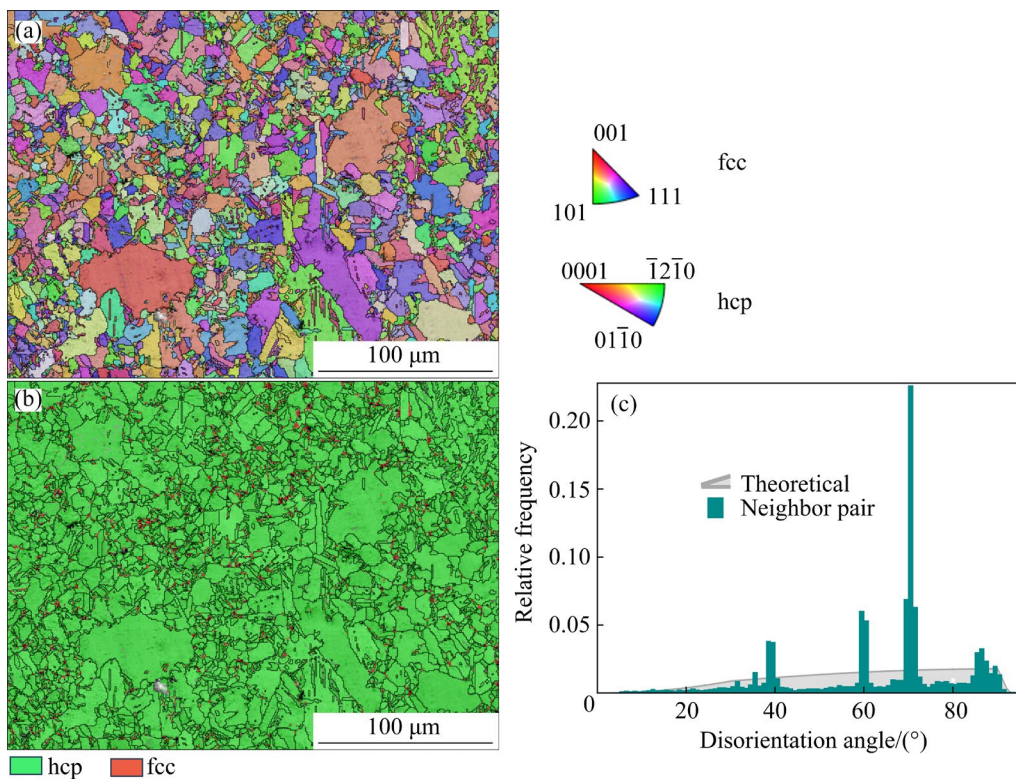


**Fig. 3** Distribution of four hcp variants along  $[011]_{fcc}$  direction (The arrow indicates the rotation between two hcp variants with the angle of 70.5°)

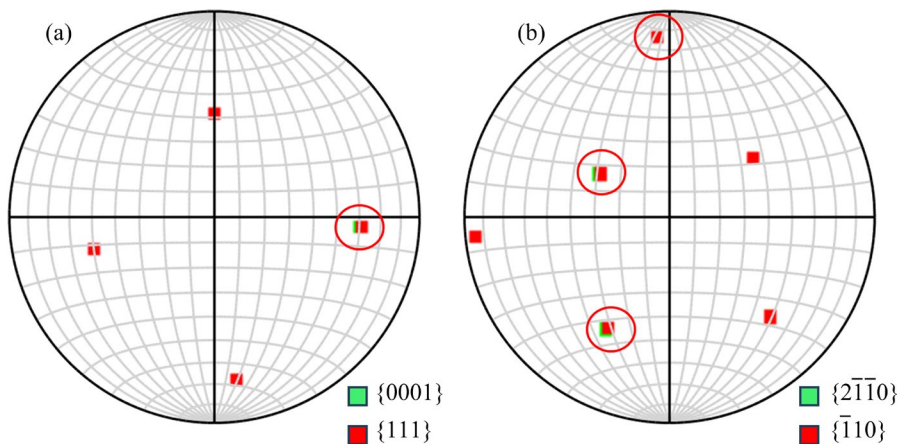
### 3.2 Crystallographic features by EBSD technique

Figure 4(a) shows the orientation mapping of the annealed sample, while Fig. 4(b) displays the phase mapping. At room temperature, the hcp structure is stable, constituting over 95% of the sample. However, due to residual fcc phase resulting from transformation delay [36], the orientation relationship between fcc and hcp phases can be directly assessed. Figure 5 shows the pole figures of the arbitrarily selected fcc phase and its neighboring hcp phase. In Fig. 5(a), a  $\{0001\}_{\text{hcp}}$  pole coincides with a  $\{111\}_{\text{fcc}}$  pole, and the

$\langle 2\bar{1}\bar{1}0 \rangle_{\text{hcp}}$  poles coincide with  $\langle \bar{1}10 \rangle_{\text{fcc}}$  poles in Fig. 5(b), indicating the well-established Shoji-Nishiyama orientation relationship between fcc and hcp phases. Figure 4(c) shows the frequency distribution of misorientation angles, which appears discontinuous and significantly deviates from the random Mackenzie distribution indicated by a grey line. The highest peak in Fig. 4(c) is at approximately  $71^\circ$  with a frequency of 23%, aligning well with the misorientation angle of  $70.5^\circ$  between the four variants deduced in Section 3.1. In addition to the peak at around  $71^\circ$ , other high-



**Fig. 4** Orientation mapping of annealed sample at 550 °C for 1 h: (a) Orientation mapping; (b) Phase mapping (Green: hcp; Red: fcc); (c) Distribution of misorientation angles



**Fig. 5** Pole figures for neighboring fcc and hcp phase: (a)  $\{0001\}_{\text{hcp}}/\{111\}_{\text{fcc}}$  poles; (b)  $\langle 2\bar{1}\bar{1}0 \rangle_{\text{hcp}}/\langle \bar{1}10 \rangle_{\text{fcc}}$  poles

frequency misorientation angles are observed at about  $32^\circ$ ,  $36^\circ$ ,  $38^\circ$ ,  $60^\circ$ ,  $71^\circ$  and  $86^\circ$ – $91^\circ$ , which have not been thoroughly explained in literature. It is noteworthy that a misorientation angle of  $60^\circ$  is evident in Fig. 4(c), and therefore, it is reasonable to suspect that this angle may originate from the twin orientations in the parent fcc structure.

### 3.3 Crystallography of residual fcc phase

In Fig. 6(a), an EBSD mapping is presented with a large magnification to provide detailed insights into the fcc phase. Figure 6(b) shows the corresponding phase mapping, where the red color highlights the fcc phase. The misorientation distribution of hcp phase is shown in Fig. 6(c), and it is similar to Fig. 4(c). Figure 6(d) shows the orientation of fcc grains, positioned along the grain boundary of hcp grains. The fcc grains exhibit diverse orientations, represented by different colors, when compared to their neighboring fcc grains. The orientation relationship between these adjacent fcc grains is analyzed through pole figures in Fig. 6(e). According to Fig. 6(e), one of  $\{111\}_{\text{fcc}}$  poles coincides with each other, and three  $\langle 011 \rangle_{\text{fcc}}$  poles on this plane also coincide. This observation indicates that the neighboring fcc grains maintain a twin orientation relationship.

Figure 7(a) shows the orientation mapping in another local area of the sample, and residual fcc grains highlighted with red color are found at the hcp grains in Fig. 7(b). The orientation of the fcc

phase is shown in Fig. 7(c), where variously oriented fcc grains are evident. By analyzing the pole figures in Fig. 7(d), the orientation relationship between neighboring fcc grains also demonstrates a twin relationship.

Figures 8(a) and (b) display reconstructed fcc orientations based on the low-temperature mapping of the hcp phase in Figs. 6(a) and 7(a), respectively [37]. The twin boundaries are highlighted in red lines. In these local areas, the twin fractions in these local areas are 42.6% and 60.1%, respectively. Nevertheless, the twin relationship in the parent fcc phase is reproducible, consistent with previous report [10]. This special orientation in the parent phase may result in different misorientation angles between transformed hcp grains, as observed in Fig. 4(c).

### 3.4 Relationship between fcc twins and their hcp variants

By supposing that two fcc grains hold a twin relationship, theoretically, four hcp variants can be generated for each fcc grain. However, one hcp variant from each fcc grain is the same, namely the hcp variants with  $\{0001\}_{\text{hcp}}$  parallel to the twin boundary. As a result, a pair of fcc twin grains can yield seven hcp variants with different orientations. Figure 9 shows variants along  $[111]_{\text{fcc}}$  direction, with labelled misorientation angles between the variants. In addition to the misorientation angle discussed in Section 3.1 ( $70.5^\circ$ ), angles of  $38.9^\circ$  and

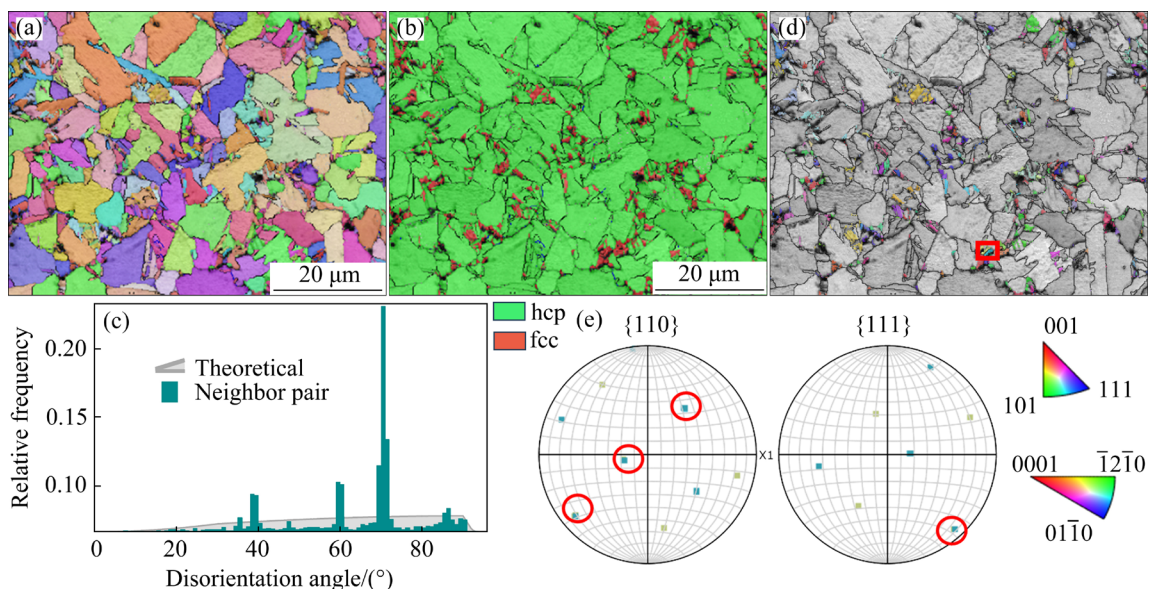


**Fig. 6** Orientation mapping of annealed sample with higher magnification: (a) Orientation mapping; (b) Phase mapping (Green: hcp; Red: fcc); (c) Distribution of misorientation angles; (d) Orientation of fcc phase; (e)  $\{110\}_{\text{fcc}}$  and  $\{111\}_{\text{fcc}}$  pole figures for fcc phase marked in (d)

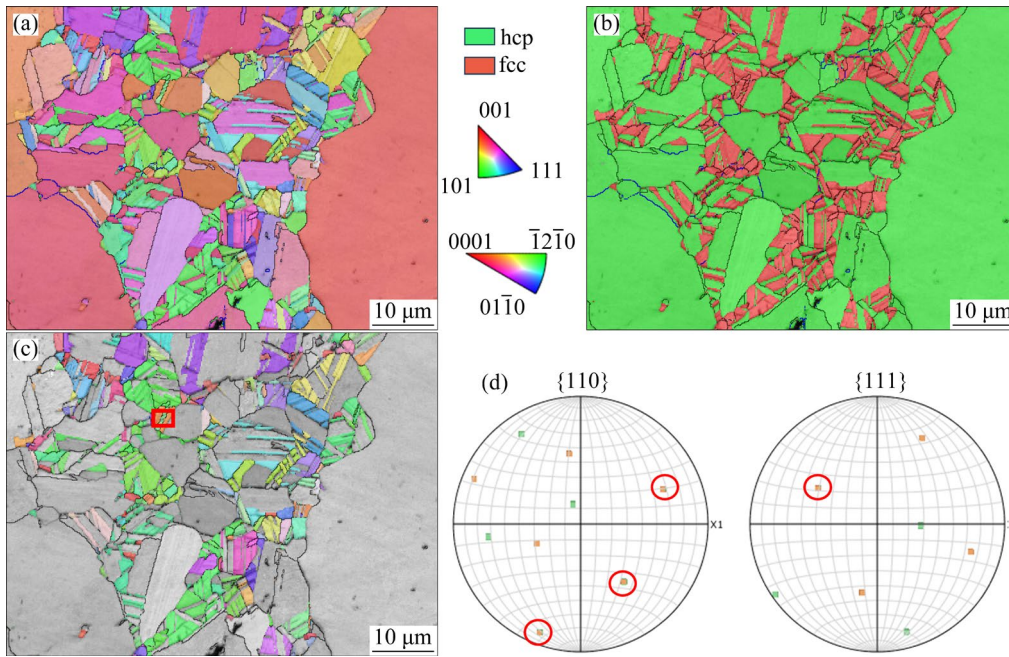


**Fig. 7** Orientation mapping of another sample: (a) Orientation mapping; (b) Phase mapping (Green: hcp; Red: fcc); (c) Orientation of fcc phase; (d) {110} and {111} pole figures for fcc phase marked in (c)

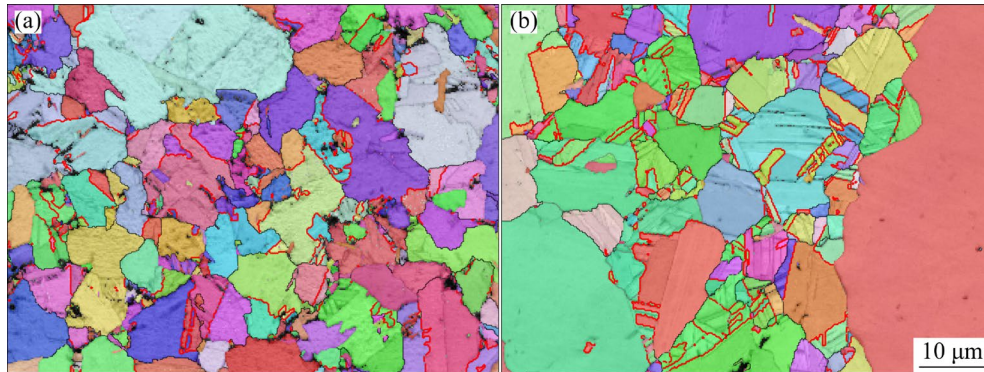


**Fig. 8** Reconstructed orientation of parent fcc phase from hcp phases (The twin boundaries are marked by red)

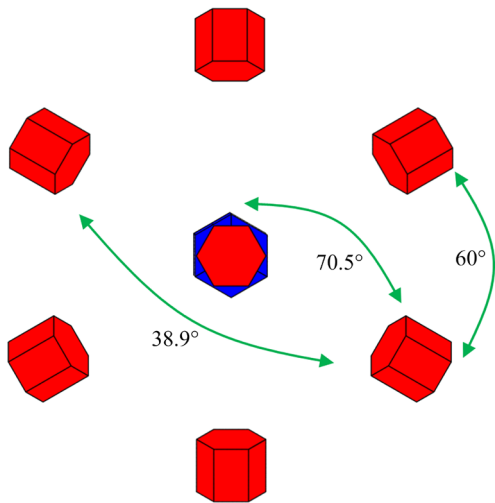


**Fig. 9** Distribution of seven hcp variants from a pair of fcc twins viewed along  $[111]_{fcc}$  direction (The  $(111)_{fcc}$  plane is twin plane)

$60^\circ$  are also identified. These angles correspond to the peaks observed in the distribution in Figs. 4(c) and 6(c). It is worth noting that the misorientation near  $38.9^\circ$  is reported to be generated in the deformation process [13], but there is such a misorientation angle before deformation.

Additionally, the misorientation angles between any two arbitrary variants from the hcp variants are calculated, and the result is given in Table 2. Twenty-eight ( $8 \times 7/2 = 28$ ) combinations for any two different variants from the eight variants are calculated. The first column in Table 2 gives the misorientation angles and the second column indicates the frequency of each angle. A  $0^\circ$  angle signifies that the pair of hcp variants are the same. The angles of  $70.5^\circ$  and  $60^\circ$  in Table 2 exhibit a

higher frequency compared to other angles, which is consistent with Figs. 4(c) and 6(c). It is noteworthy that there are additional misorientation angles, such as 32°, 36° and 86°–91°, which lack a clear rationale, although their frequency is lower compared to the peaks observed for 60° and 71°.

**Table 2** Misorientation angles between arbitrary two of eight hcp variants and their appearance counts

Misorientation angle/(°)	Appearance count from 28 pairs
0	1
38.9	3
60	6
70.5	18

Since only a pair of fcc twins are considered above, there are four fcc twin variants in total, corresponding to the twinning planes of  $(111)_{\text{fcc}}$ ,  $(\bar{1}11)_{\text{fcc}}$ ,  $(1\bar{1}1)_{\text{fcc}}$ , and  $(11\bar{1})_{\text{fcc}}$ . When taking into account the four hcp variants from each fcc grain, a total of sixteen variants can be generated. The misorientation angle between any two arbitrary variants out of these sixteen variants is calculated and the results are presented in Table 3. Compared to Table 2, additional misorientations such as 31.5°, 35.4° and 89.8° are identified, and these align well with the peaks observed in Figs. 4(c) and 6(c). Furthermore, the frequency of each misorientation angle is given in the second column of Table 3. The misorientation angle of 70.5° exhibits the highest frequency, followed by the angle of 60°, consistent with the observations with the EBSD technique.

**Table 3** Misorientation angles between arbitrary two of hcp variants generated from four fcc twins and their appearance counts

Misorientation angle/(°)	Appearance count from 190 pairs
0	4
31.5	6
35.4	12
38.9	24
60	48
67	12
70.5	60
89.8	24

Figure 10 presents a quantitative comparison between the experimentally observed and theoretically predicted frequencies of misorientation angles. This comparison assumes that the total fraction of these special angles is equal to 1, and all variants appear with equal possibility. Notably, the experimentally observed frequency of 70.5° misorientation angle in Fig. 10 is larger than the theoretical prediction. This discrepancy might be attributed to the factors, such as the grain size, and nucleation sites, which have not been taken into account in Fig. 10.

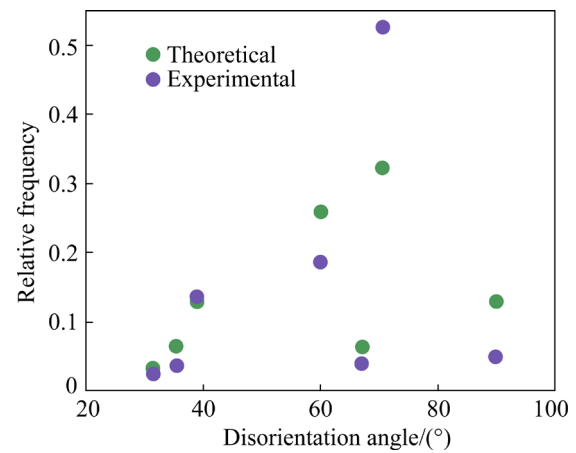


**Fig. 10** Comparison between experimental and theoretical frequency in misorientation angles

To summarize, the special orientation angles other than 70.5° are attributed to fcc twinned grains. In an extreme case where only one fcc single crystal or randomly oriented fcc grains are considered, the misorientation would be 100% of 70.5° according to the deduction in Section 3.1. However, when twinned fcc is considered, as given in Tables 2 and 3, the fraction of 70.5° grain boundaries is reduced to about 1/3. The relative fraction of 70.5° among the special misorientation angles observed in Fig. 10 is about 52% (of all special misorientations), indicating that the high-temperature fcc grains in this sample contain twins. Otherwise, only the 70.5° misorientation should be observed. The twinned fraction in parent fcc could be estimated as

$$f = \frac{1 - 0.52}{1 - 1/3} = 72\% \quad (1)$$

This estimation is slightly higher than the twin grain fraction of 61.63% in Fig. 8(a), but it provides a relatively good approximation. Compared to the parent reconstruction method [37–39], estimation

from the misorientation angles is simpler and requires fewer computation resources.

The origins of twins in the parent fcc grains can be attributed to several factors. One possible reason for the grown twin is due to a low stacking fault energy [8], which is  $(27\pm 4)$  mJ/m<sup>2</sup> as reported before [14]. Another source of the twined fcc is the hcp→fcc transformation. During the heating of the hcp phase to the transformation temperature, the hcp→fcc transformation occurs. The Shoji–Nishiyama orientation relationship is still preserved between two phases, as shown in Fig. 11, indicating two fcc variants originating from a single hcp phase based on this orientation. These two fcc variants maintain a twin relationship, suggesting that the twin in high-temperature fcc grains may also result

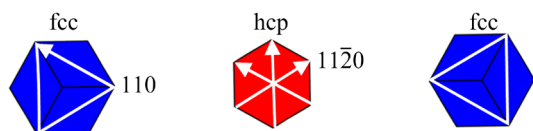


Fig. 11 Two fcc variants from hcp→fcc transformation

from the transformation twin variants, in addition to the grown twin. Further insight into the formation of fcc twins could be gained through in-situ observation.

Figure 12 shows an in-situ EBSD test result capturing the hcp→fcc transformation. The microstructure before heating is shown in Figs. 12(a, b), consisting of a fully hcp phase. This sample contains nearly {0001} grains generated by the recrystallization below the phase transformation temperature, and this deliberate selection helps avoid the presence of pre-existing special misorientation angles due to phase transformation, which might otherwise be inherited in the subsequent transformation. Upon heating the sample to 450 °C, the corresponding EBSD results are shown in Figs. 12(c, d), and hcp→fcc transformation occurs according to the phase mapping in Fig. 12(d). Lamellar structures of the fcc phase are formed within in the hcp grains, as shown in Fig. 12(c). The twin boundaries in Fig. 12(c) are highlighted by red lines in Fig. 12(e),

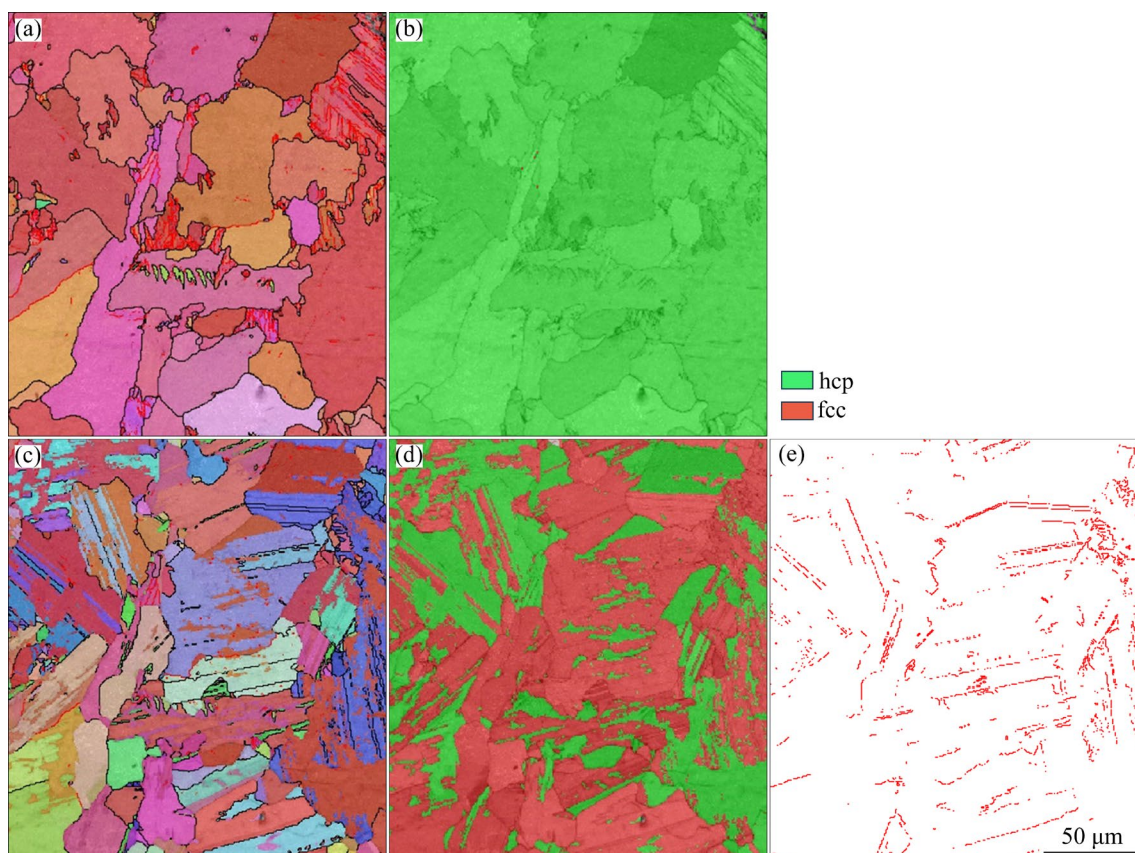
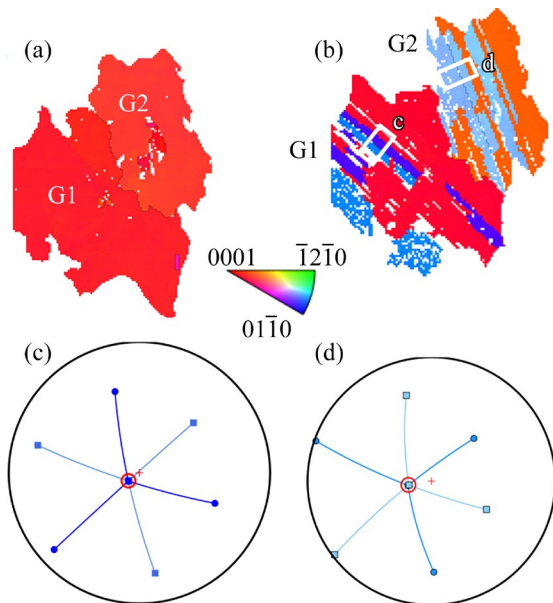


Fig. 12 Orientation mapping of sample with in-situ EBSD test: (a) Orientation mapping before heating; (b) Phase mapping of (a) (Green: hcp; Red: fcc); (c) Orientation mapping after heating; (d) Phase mapping of (c); (e) Twin boundaries between fcc phase in (c, d) shown in red colors

and their fraction is as high as 70.3%, which is close to the estimation of 72% based on the misorientation angles.

Two grains in Figs. 12(a, c) are selected for further analysis and presented in Fig. 13. The two grains are labelled as G1 and G2, respectively. From Figs. 13(a, b), the lamellar fcc phase is formed upon heating. The orientation of the fcc lamella, marked by rectangles in Fig. 13(b), is demonstrated in Figs. 13(c, d) using  $\{111\}_{\text{fcc}}$  pole figures. Four  $\{111\}_{\text{fcc}}$  poles of one fcc grain are connected with line segments. A pair of fcc grains are observed in both G1 and G2. According to the pole figure, the two fcc grains are related by a twin relationship, and the shared  $\{111\}$  pole coincides with the  $\{0001\}_{\text{hcp}}$  pole indicated by red circles in Figs. 13(c, d). Figure 11 suggests that twinned fcc grains can be formed by hcp→fcc transformation, and this is consistent with present in-situ observation.



**Fig. 13** Orientation mappings of two selected grains before (a) and after (b) heating, and  $\{111\}$  pole figures (c, d) for fcc phase marked in (b)

In addition, it is noted that the twins are formed in pairs, which is a typical microstructure generated by phase transformation. During the hcp→fcc transformation, operation of  $1/3\langle 10\ 10 \rangle_{\text{hcp}}$  partial dislocations can transform the hcp structure to the fcc structure, and the shear strain due to the partial shears can increase the strain energy in the system. However, the formation of twinned fcc

pairs with opposite shears can reduce the total strain energy, which is known as strain accommodation [40,41]. Therefore, the in-situ EBSD test demonstrates that the twinned structures in fcc grains result from phase transformation. Moreover, the profuse twinned structures are crucial for grain boundary engineering (GBE) [42], and the present result could also be applied to the GBE through the hcp↔ fcc phase transformation process.

## 4 Conclusions

(1) There are four Shoji–Nishiyama variants for hcp variants formed from a single fcc matrix. The misorientation angle between the variants is  $70.5^\circ$  and the rotation axis is  $\langle 11\bar{2}0 \rangle$  in hcp and  $\langle 011 \rangle$  in the fcc matrix.

(2) The misorientations with the statistical significance, other than  $70.5^\circ$ , are identified, and they are attributed to the twinned fcc matrix. The analysis of hcp variants resulting from four fcc twins agrees well with the EBSD results.

(3) A method to estimate the fcc twin fractions is proposed based on the special misorientation angles and the predicted results show relatively good agreement with in-situ observation.

(4) The twin can originate from two origins. One is due to the low stacking fault energy, and the other is due to the twin variants from the hcp→fcc transformation. The latter scenario is directly verified by the in-situ EBSD test.

### CRedit authorship contribution statement

**Jin-jiang HE:** Conceptualization, Methodology, Investigation, Writing – Original draft; **Guo-jin XU:** Data curation, Writing – Review & editing; **Xing-quan WANG:** Investigation, Formal analysis, Writing – Review & editing; **Jun-feng LUO:** Funding acquisition, Investigation, Resources, Writing – Review & editing; **Dan LIU:** Data curation, Writing – Review & editing; **Yong-jun LI:** Investigation, Writing – Review & editing; **Xin-fu GU:** Supervision, Formal analysis, Resources, Writing – Review & editing.

### Declaration of competing interest

The authors declare that they have no known competing financial interests or personal relationships that could have appeared to influence the work reported in this paper.

## Data availability

The data that support the findings of this study are available from the corresponding author upon reasonable request.

## Acknowledgments

This work was financially supported by the National Key R&D Program of China (No. 2022YFB3504403).

## References

- [1] SATO J, OMORI T, OIKAWA K, OHNUMA I, KAINUMA R, ISHIDA K. Cobalt-base high-temperature alloys [J]. *Science*, 2006, 312: 90–91.
- [2] WU Chang-hong, HAN J H, SHI Xing-zhao, KOLI D R, PENIGALAPATI D. Cobalt CMP development for 7 nm logic device [J]. *ECS Transactions*, 2017, 77: 93–97.
- [3] DUTTA S, BEYNE S, GUPTA A, KUNDU S, van ELSHOCHT S, BENDER H, JAMIESON G, VANDERVORST W, BÖMMELS J, WILSON C J. Sub-100 nm<sup>2</sup> cobalt interconnects [J]. *IEEE Electron Device Letters*, 2018, 39: 731–734.
- [4] DEE K C, PULEO D A, BIZIOS R. An introduction to tissue-biomaterial interactions [M], New Jersey: John Wiley & Sons, 2003.
- [5] CHRISTIAN J W. A theory of the transformation in pure cobalt [C]//Proceedings of the Royal Society of London: Series A. Mathematical and Physical Sciences, 1951, 206: 51–64.
- [6] NISHIYAMA Z. Martensitic transformation [M]. New York: Elsevier, 1978.
- [7] BAUER R, JÄGLE E A, BAUMANN W, MITTEMEIJER E J. Kinetics of the allotropic hcp-fcc phase transformation in cobalt [J]. *Philosophical Magazine*, 2011, 91: 437–457.
- [8] CHRISTIAN J W. The theory of transformation in metals and alloys [M]. Oxford: Pergamon Press, 2002.
- [9] PORTER D A, EASTERLING K E, SHERIF M Y. Phase transformations in metals and alloys [M]. 4th ed. Boca Raton: CRC press, 2021.
- [10] TU Jian, ZHANG Song-quan, ZHOU Tao, TANG Hai-long, ZHOU Zhi-ming. Structural characterization of island  $\epsilon$ -martensitic plate in cobalt [J]. *Materials Characterization*, 2016, 119: 34–39.
- [11] KHLEBNIKOVA Y V, TABATCHIKOVA T, RODIONOV D, SAZONOVA V. Crystallographic aspects of structure formation under the  $\beta \rightarrow \alpha$  transformation in oriented cobalt single crystals [J]. *Bulletin of the Russian Academy of Sciences: Physics*, 2009, 73: 1207–1210.
- [12] TU Jian, MENG Xing, ZHOU Zhi-ming, HUANG Can. Effects of holding time, cooling rate and predeformation on microstructural characteristics of cobalt undergoing  $\gamma \rightarrow \epsilon$  transformation [J]. *Chinese Journal of Nonferrous Metals*, 2018, 28: 97–106. (in Chinese)
- [13] LIU Wei-jing, AN Xing-long, JIANG Wen-ting, NI Song, SONG Min. Microstructural evolution of a polycrystalline cobalt during tensile deformation [J]. *Materials Science and Engineering A*, 2021, 826: 141970.
- [14] AN Xing-long, LI Yan, NI Song, WANG Zhang-wei, SONG Min. Grain refinement process in a cold-rolled polycrystalline cobalt [J]. *Materials Characterization*, 2020, 164: 110360.
- [15] AN Xing-long, LI Yan, NI Song, WANG Zhan-wei, SONG Min. Microstructural and hardness evolutions of a cold-rolled cobalt [J]. *Materials Science and Engineering A*, 2021, 803: 140712.
- [16] ZHU Yun-tian, ZHANG Xi-yan, LIU Qing. Observation of twins in polycrystalline cobalt containing face-center-cubic and hexagonal-close-packed phases [J]. *Materials Science and Engineering A*, 2011, 528: 8145–8149.
- [17] GUO Shen-da, BAO Rui., YANG Ping, LIU Liang, YI Jian-hong. Morphology and carbon content of WC-6%Co nanosized composite powders prepared using glucose as carbon source [J]. *Transactions of Nonferrous Metals Society of China*, 2018, 28: 722–728.
- [18] WU Xiao-lei, TAO Nai-rong, HONG You-shi, LIU Gang, XU Bing-she, LU Jian, LU Ke. Strain-induced grain refinement of cobalt during surface mechanical attrition treatment [J]. *Acta Materialia*, 2005, 53: 681–691.
- [19] SONG Ke-rui, LI Zhou, FANG Mei, XIAO Zhu, ZHU Yun-tian, LEI Qian. Recrystallization behavior and phase transformation in a hot-rolled pure cobalt during annealing at the elevated temperature [J]. *Materials Science and Engineering A*, 2022, 845: 143178.
- [20] RÉMY L, PINEAU A. Twinning and strain-induced f.c.c.  $\rightarrow$  h.c.p. transformation on the mechanical properties of Co-Ni-Cr-Mo alloys [J]. *Materials Science and Engineering*, 1976, 26: 123–132.
- [21] GARCÍA J S, MEDRANO A M, RODRÍGUEZ A S. Effect of solution treatments on the FCC/HCP isothermal martensitic transformation in Co-27Cr-5Mo-0.05C aged at 800 °C [J]. *Scripta Materialia*, 1999, 40: 717–722.
- [22] MANI A, LOPEZ H. Deformation induced FCC to HCP transformation in a Co-27Cr-5Mo-0.05C alloy [J]. *Materials Science and Engineering A*, 2011, 528: 3037–3043.
- [23] OLSON G B, COHEN M. A general mechanism of martensitic nucleation. Part I: General concepts and the FCC  $\rightarrow$  HCP transformation [J]. *Metallurgical Transactions A*, 1976, 7: 1897–1904.
- [24] YANG Xu-sheng, SUN Sheng, RUAN Hai-hui, SHI San-qiang, ZHANG Tong-yi. Shear and shuffling accomplishing polymorphic fcc  $\gamma \rightarrow$  hcp  $\epsilon \rightarrow$  bct  $\alpha$  martensitic phase transformation [J]. *Acta Materialia*, 2017, 136: 347–354.
- [25] ARISTEIDAKIS J S, HAIDEMENOPOULOS G N. Constitutive and transformation kinetics modeling of  $\epsilon$ -,  $\alpha'$ -Martensite and mechanical twinning in steels containing austenite [J]. *Acta Materialia*, 2022, 228: 117757.
- [26] CHEN Si-jing, OH H S, GLUDOVATZ B, KIM S J, PARK E S, ZHANG Ze, RITCHIE R O, YU Qian. Real-time observations of TRIP-induced ultrahigh strain hardening in a dual-phase CrMnFeCoNi high-entropy alloy [J]. *Nature Communications*, 2020, 11: 826.
- [27] PARK H D, WON J W, MOON J, KIM H S, SUNG H, SEOL J B, BAE J W, KIM J G. Fe<sub>55</sub>Co<sub>17.5</sub>Ni<sub>10</sub>Cr<sub>12.5</sub>Mo<sub>5</sub> high-entropy alloy with outstanding cryogenic mechanical properties driven by deformation-induced phase

- transformation behavior [J]. *Metals and Materials International*, 2023, 29: 95–107.
- [28] MA Zi-hao, BING Hou, QIN Dong-yang, LI Yu-long, Effect of strain rate on mechanical properties of HCP/FCC dual-phase CoCrFeNiNb<sub>0.5</sub> high-entropy alloy [J]. *Transactions of Nonferrous Metals Society of China*, 2023, 33: 1144–1155.
- [29] UPADHYAYA G S, Materials science of cemented carbides—An overview [J]. *Materials & Design*, 2001, 22: 483–489.
- [30] ZHU Er-tao, ZHANG Jiu-xing, GUO Sheng-da, YANG Xin-yu, ZHANG Xiang, YANG Jian-gao. Effect of Co on morphology and preparation of in situ synthesis of WC–Co composite powders [J]. *Materials Research Express*, 2019, 6: 086522.
- [31] YE Xiao-yuan, XIANG Cong-ying, NIE Hong-bo, LEI Hua-sheng, DU Yong, XING Wan-dong, LUO Jian, YU Zhi-yang. Facet-dependent interfacial segregation behavior of V-doped WC–Co cemented carbides [J]. *Ceramics International*, 2022, 48: 11251–11256.
- [32] GU Xin-fu, FURUHARA T, ZHANG Wen-zheng. PTCLab: Free and open-source software for calculating phase transformation crystallography [J]. *Journal of Applied Crystallography*, 2016, 49: 1099–1106.
- [33] CAYRON C. The transformation matrices (distortion, orientation, correspondence), their continuous forms and their variants [J]. *Acta Crystallographica Section A: Foundations and Advances*, 2019, 75: 411–437.
- [34] ARNOLD R, JUPP P, SCHAEFEN H. Orientation relationships, orientational variants and the embedding approach [J]. *Journal of Applied Crystallography*, 2023: 56: 725–736.
- [35] RANDLE V. Microtexture determination and its applications [M]. London: CRC Press, 2003.
- [36] ISKOUNEN N, DUBOS P, FAJOUJ J, CORET M, MOYA M, GIRAULT B, BARRIER N, BRUZY N, HUG E, GLOAGUEN D. Experimental investigation of allotropic transformation of cobalt: influence of temperature cycle, mechanical loading and starting microstructure [J]. *Metallurgical and Materials Transactions A*, 2021, 52: 1477–1491.
- [37] HUANG Cheng-yao, NI Hsu-chih, YEN Hun-wei. New protocol for orientation reconstruction from martensite to austenite in steels [J]. *Materialia*, 2020, 9: 100554.
- [38] CAYRON C. ARPGE: A computer program to automatically reconstruct the parent grains from electron backscatter diffraction data [J]. *Journal of Applied Crystallography*, 2007, 40: 1183–1188.
- [39] MIYAMOTO G, IWATA N, TAKAYAMA N, FURUHARA T. Reconstruction of parent austenite grain structure based on crystal orientation map of Bainite with and without Ausforming [J]. *ISIJ International*, 2011, 51: 1174–1178.
- [40] GU Xin-fu, FURUHARA T, KIGUCHI T, KONNO T J, CHEN Leng, YANG Ping. Strain self-accommodation during growth of 14H type long-period stacking ordered (LPSO) structures in Mg–Zn–Gd alloy [J]. *Scripta Materialia*, 2020, 185: 25–29.
- [41] FURUHARA T, GU Xin-fu. Discussion on strain accommodation associated with formation of LPSO Structure [J]. *Materials Transactions*, 2013, 54: 675–679.
- [42] WATANABE T. Grain boundary engineering: Historical perspective and future prospects [J]. *Journal of Materials Science*, 2011, 46: 4095–4115.

## 纯 Co 中 fcc→hcp 转变的取向差来源及原位验证

何金江<sup>1,2</sup>, 徐国进<sup>1,2</sup>, 王兴权<sup>3</sup>, 罗俊峰<sup>1,2</sup>, 刘丹<sup>1,2</sup>, 李勇军<sup>1,2</sup>, 顾新福<sup>4</sup>

1. 有研亿金新材料有限公司, 北京 102200;
2. 北京高纯金属溅射靶材技术研究中心, 北京 102200;
3. 中国有研集团, 北京 102200;
4. 北京科技大学 材料科学与工程学院, 北京 100083

**摘要:** 通过电子背散射衍射表征方法和相变晶体学模型, 阐明了纯钴中面心立方(fcc)结构转变到密排六方(hcp)结构后取向差的来源。结果发现, fcc→hcp 相变过程中 Shoji–Nishiyama 位向关系产生 4 个变体, 变体之间的取向差角为 70.5°, 旋转轴为 (11 $\bar{2}$ 0), 为实验中主要观察到的取向差。另外, 还观察到 hcp 晶粒之间其他占有重要比例的取向差, 包括 32°, 36°, 38°, 60°, 71° 和 86°~91°。这些新观察到的取向差与高温母相的显微组织密切相关。母相中存在的孪晶结构是形成这些特殊取向差的原因。此外, 还提出了一种基于取向差分布估算 fcc 孪晶分数的方法, 预测结果与实验观察较吻合。原位 EBSD 观察证明 fcc 中的孪晶来源于 hcp→fcc 相变。

**关键词:** 钴; 相变晶体学; 变体; 位向关系; 孪晶

(Edited by Bing YANG)